Journal: *Journal of Mass Spectrometry*

Title: Study of solid/gas phase photocatalytic reactions by electron ionisation mass spectrometry

Author: Manuel Nuño, Richard Ball, Chris R. Bowen

Architecture and Civil Engineering department, University of Bath, Claverton down BA2 7AY

Mr. Manuel Nuño: m.nuno@bath.ac.uk, 0044 7588959162

Dr Richard Ball: r.j.ball@bath.ac.uk, 0044 (0)1225 386944

Prof Chris Bowen: c.r.bowen@bath.ac.uk, 0044 (0) 1225 383660

Abstract

This paper describes a novel methodology for the real time study of solid-gas phase photocatalytic reactions in-situ. A novel reaction chamber has been designed and developed to facilitate the investigation of photoactive materials under different gas compositions. UV irradiation in the wavelength of ranges 376-387 and 381-392 nm was provided using specially designed high efficiency light emitting diode (LED) arrays. The experiments used air containing 190 ppm NO_2 in a moist environment with a relative humidity (RH) of 0.1. Photocatalytic samples consisting of pressed pellets of rutile and anatase crystalline forms of TiO_2 were monitored over a period of 150 minutes. A ultra-high vacuum right angled bleed valve allowed a controlled flow of gas from the main reaction chamber at atmospheric pressure to a residual gas analyser (RGA) operating at a vacuum of 10^{-5} mbar. The apparatus and methodology have been demonstrated to provide high sensitivity (ppb). The rate of degradation of NO_2 attributed to reaction at the TiO_2 surface was sensitive to both crystal structures (anatase or rutile) and wavelength of irradiation.

Highlights

- A novel methodology for the study of solid/gas phase photocatalytic reactions by electron ionisation mass spectrometry is described.
- Variations in photocatalytic activity of TiO_2 substrates due to crystal structure and UV irradiation has been detected using mass spectrometry.
- Real time gas phase photoactivity of two titanium dioxide polymorphs is reported using a methodology which allows, changes in a range of mass-to-charge ratio involving H_2O, N_2, O_2, Ar, CO_2 and NO_2 species to be studied. This presents a significant step forward compared to liquid based methods.

Keywords
photocatalysis; UV irradiation; nitrogen dioxide; pollutant; residual mass analyser; mass spectrometer

Abbreviations

λ = wavelength

A=ampere

Ar = argon

a.m.u. = atomic mass unit

a.u.= arbitrary unit

CO_2 = carbon dioxide

e_{cb}^- = electron conduction band

FT-IR = Fourier transform infra-red spectroscopy

GaN = gallium nitride

h_{vb}^+= hole valence band

H_2O = water

LED = light emitting diode

mbar=milibar

m/z=mass-to-charge ratio

N_2 = nitrogen

NO_2 = nitrogen dioxide

NOx = nitrogen oxides

O_2 = oxygen

RGA = residual gas analyser

TiO_2 = titanium dioxide

UV = ultra violet

VOC = volatile organic compound

Introduction

An increasing global population and increasing demand on resources and energy supply has led to a greater awareness of pollution and air quality. The monitoring of air pollution emissions is becoming more widespread, especially in cities where a high density of cars and houses increase the concentration of VOCs such as nitrogen oxides and sulphur dioxide. These pollutants are not only linked to climate change[1], they also present serious health hazards for the population through increased risk of developing respiratory diseases and cancer [2, 3]. For this reason the European Union and United States have developed legislation to establish standards and objectives to control air quality in order to improve environmental and atmospheric conditions. Environmental standards for SO_2 were introduced in 2005 and NO_2 standards were introduced later in 2010 [4].

Since the initial experiments by Fujishima and Honda in 1972 with titanium dioxide [5], interest in photocatalytic materials has continually increased and they are considered today as an important tool for pollution remediation [6] and neutralisation of pathogens because of their antibacterial and antifungal properties [7-10]. Photocatalysts are semiconductors with the ability to create free radicals in the presence of UV light [5, 11-13] by the promotion of electrons from the valence band to the conduction band. This process generates a reactive hole (h_{vb}^+) on the surface of the crystal and this electron-hole pair can react with moisture to provide free radicals. TiO_2 has three different natural polymorphs: rutile, anatase and brookite. This study will address surface reactions on the two most common forms, rutile and anatase. Rutile is the most stable crystal structure with a band gap of 3.0eV [14-16], whereas the band gap of anatase is higher, 3.2eV [16, 17]. Current theories identify the band gap as the primary reason that anatase is more effective to promote photocatalytic reactions compared to rutile [18].

The reaction scheme described by equations 1 to 6 shows the initial creation of electron hole pairs on the TiO_2 surface (1) followed by the creation of free radicals, which promote the reduction-oxidation (redox) processes responsible for the removal of hazardous molecules.

$$TiO_2 + h\nu \rightarrow h_{vb}^+ + e_{cb}^- \quad (1)$$

$$h_{vb}^+ + H_2O \rightarrow \bullet OH + H^+ \quad (2)$$

$$e_{cb}^- + H^+ \rightarrow \bullet H \quad (3)$$

$$e_{cb}^- + O_2 \rightarrow O_2^{\bullet -} \quad (4)$$

$$h_{vb}^+ + O_2^{\bullet -} \rightarrow {}^1O_2 \quad (5)$$

$$H^+ + O_2^{\bullet -} \rightarrow HO_2^{\bullet} \quad (6)$$

Water is required in reaction 2 to produce a hydroxyl radical and H^+. The H^+ then reacts as shown in reaction 6 to produce a peroxyl radical (which is involved in the formation of hazardous molecules) in reaction 6, however this oxidizing specie is not responsible for the primary oxidation of substances such as volatile organic molecules (VOC's); such a process requires initiation by holes [19, 20]. Fujishima, Hoffmann, Heller and Serratos concluded that molecular oxygen (reaction 5) is the primary species in the environmental clean-up reaction [12, 19, 21, 22]. Oxygen traps the generated electrons (reaction 4),

displacing the equilibrium charge generation/charge recombination to the separation of charges (holes and electrons) [23]. Although singlet oxygen is generated, it deactivates through electron transfer [24].

Researchers have studied photocatalysts for many purposes and recent development of paints and coatings [10, 25-27] for the environmental remediation in both indoor and outdoor urban areas has been identified as a promising field on research.

Currently the majority of experimental work carried out to measure photoactivity involves the photocatalytic degradation of an organic dye in an aqueous liquid phase [28-38]. This experimental approach does not require expensive facilities and results are relatively straight forward to interpret. Although the use of organic dyes is widely accepted among the academic community it is problematic to extrapolate those results to a gas phase reaction, as is the case with atmospheric pollutants. This is due to the involvement of different mechanisms such as the adsorption process. In addition, the low concentration of many pollutants, such as NO_2 in particular, increases the difficulty to analyse their degradation.

Alternative approaches which are able to monitor gas phase reactions utilise novel detectors based on a modified gas chromatography system with chemiluminescent detection for NO_2 and peroxyacyl nitrates [39] or the use of a Fourier transform infra-red spectroscopy (FTIR) to follow the photo decomposition of nitrogen monoxide [40]. The major limitation of these approaches is the exclusivity of the analysis technique to one or two species or a relatively low detection limit. The major advantage of using a residual gas analyser, which is used in this paper, is the ability to detect multiple species in the working mass-to-charge range.

The apparatus and methodology described in this paper provide an alternative tool for those studying photocatalysis of TiO_2 in the gas phase and provides an effective method of monitoring the degradation of CO_2 and NO_2.

Experimental

A schematic diagram of the apparatus is shown in Figure 1. The system comprises of several elements including a 203ppm of NO_2 diluted in N_2 gas cylinder, zero air grade gas cylinder, flowmeters, humidifier, reaction chamber, UV source, rotary pump, UHV right angled valve, turbomolecular pump, low pressure RGA system, data logging and data analysis.

A Microvision 2 residual gas analyser (RGA) was supplied by MKS Instruments Inc. The ion source consisted of a thoriated tungsten filament that ionised the sample by electron impact followed by a quadrupole to separate the ions. A standard dual detection was provided through a Faraday cup detector for minimum partial pressure detection of 10^{-11} mbar and a microchannel plate electron multiplier that amplified the signals by the multiplication of electrons for detection up to 10^{-14} mbar partial pressures. The sensitivity of 0.45A/mbar was achieved through operation of the ion source with an emission current of 1mA, electron energy 70eV and ion energy of 5.5mA. From a possible scanning range between 1 and 100 mass to charge ratio (m/z) these experiments employed a range from 14m/z to 70m/z with a step size of 0.12m/z scanning 8 points per amu (taking less than $3x10^{-3}$s per point), thereby increasing the frequency at with data that could be collected.

Gas flows were regulated using flow meters capable of measuring gas flows from 5cm^3/min to 100cm^3/min (Platon Gap meter Type NGX supplied by Roxspur Measurement & Control Ltd). Two different gas cylinders were supplied by BOC Gases Ltd, a zero air grade (of composition H_2 0.5ppm, He 2ppm, CH_4 1ppm, H_2O<5ppm, Ne 5ppm, O_2 ~20.95%, Ar 9300ppm, CO_2 385ppm, N_2O 0.8ppm, balance N_2), and 203ppm of NO_2 diluted in N_2.

The reaction chamber gas composition was controlled by adjusting the input flow via flow meters and mixing them with compressed air. A Pyrex glass bubbler filled with distilled water connected to the compressed air was used to humidify the gas inside the chamber. Stainless steel pipes provided good corrosion resistance from the NO_2 and were connected using ¼ inch Swagelok® connections. The reaction chamber was designed to operate at different pressures (10^3-10^{-6} mbar), temperatures (0 -40°C) and gas compositions (0-203ppm of NO_2 and different relative humidity). The chamber consists of a stainless steel (grade 304) chamber (6-way cross) with a volume of 290cm^3 in which an input pipe delivered the desired gas composition and an output pipe connected to the residual gas analyser through a right angled valve and an UHV right angled bleed valve to reduce the pressure to 10^{-5} mbar. An additional output valve connects the chamber to a secondary rotary pump (Adixen 2010SD) to achieve low vacuum conditions inside the chamber before each experiment, this mitigated against incomplete replacement of gas in the chamber caused by 'dead zones'. The right angled valve isolated the entry of gas to the detector through the UHV angled valve when the secondary pump was in operation, and was in the fully opened position when the reaction occurs. All the joints were sealed using vacuum ConFlat flanges with silver coated copper gaskets. A metering valve was installed to provide an exhaust from the chamber.

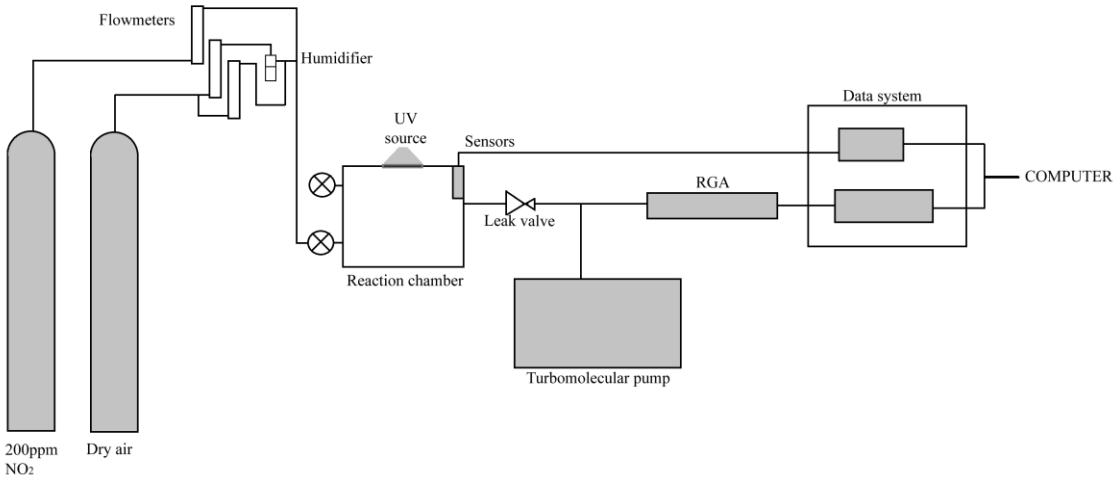

Figure 1. *Diagram of the system showing how the gas cylinders are connected to the reaction chamber through flowmeters and valves. The reaction chamber has four connections, one input valve connected to the gases, one output valve connected to the detector, one purge valve connected to the rotary pump and one exhausting valve. The detector is connected to a computer.*

Prior to carrying out experimental work all internal surfaces of the reaction chamber were passivated by exposure to 200ppm of NO_2 diluted in N_2 for 72 hours. Irradiation of the sample inside the chamber

was provided through an optical quartz glass viewport which provided a transmission greater than 99.9% at λ360nm which increased to 100% at λ 400nm. Prior to initiating the experiment, the intensity of UV light provided by an LED array was measured using a Delta Ohm photo-detector model LP471 UVA (radiometric probe optimised for measuring the irradiance in the UVA range) after it had passed through the quartz window. The wavelength range extended from 315nm to 400nm with and accuracy of $10^{-4}W/m^2$ (model LP471 UVA provided by Delta Ohm).

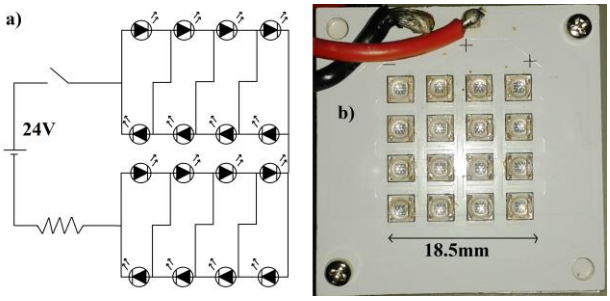

Figure 2. *Diagram of the circuit (a) and picture of the built LED (b).*

Two different UV LED arrays were fabricated specifically for these experiments. Each UV source comprised of a 4 x 4 array of 16 individual GaN UV-LED's. Operation was carried out at a voltage from 15.4 to 15.8V, a current of 1400mA at 40°C. LED's 3.5 mm in diameter were mounted at a spacing of 1.5mm. The LED's of wavelength 376-387nm provided a maximum intensity at 380nm with a total intensity of 30.4 W/m^2; whereas the LED's of wavelength 381-392nm emitted the maximum intensity at 386nm with a total intensity of 40.8 W/m^2. Figure 2 shows a diagram of the LEDs arrays and corresponding spectra are shown in Figure 3.

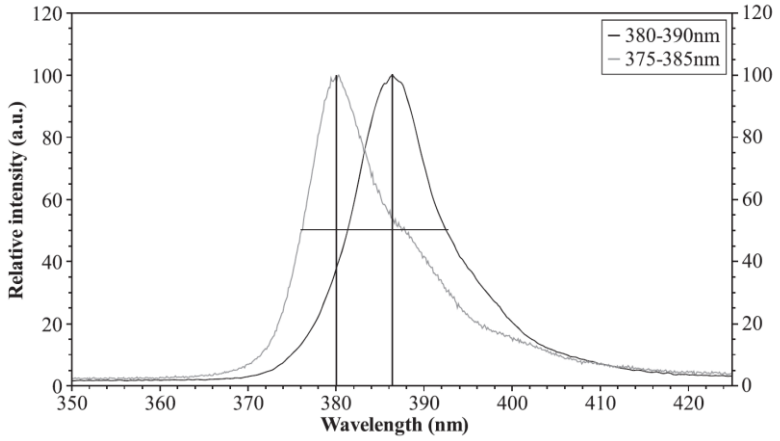

Figure 3. S*pectra of LED arrays. Wavelength ranges of 376-387nm and 381-392nm calculated at full width half maximum (FWHM).*

Materials and methods

Two grades of titanium dioxide were used;

(i) Anatase in the form of Aeroxide® P25 from Sigma Aldrich (≥99.5% trace metals basis, average particle size 21nm and a surface area from $35m^2/g$ to $65m^2/g$)
(ii) Rutile in the form of TiPure® R-960 with a particle size of 500nm supplied by DuPont.

Prior to photocatalytic evaluation of the materials their crystalline phases were analysed using a Renishaw inVia Raman microscope equipped with an excitation laser at 532nm. This showed that both grades of titanium dioxide were pure anatase and pure rutile. These results were corroborated by subsequent analysis using XRD diffraction which was carried out using a D8 ADVANCE X-ray diffractometer with Cu_α radiation, 2θ with a step of 0.016° and a step time of 269s. Results are shown in figures 4 and 5.

A mass of 0.5g of each powder was cold pressed into individual pellets 13mm in diameter under a pressure $69x10^3N/m^2$. The experiments were carried out at 25°C and atmospheric pressure for 150 minutes inside the chamber, whereas the mass spectrometer operated at a pressure of $5.4x10^{-5}$ mbar in the low pressure side of the apparatus. Both LED's operated with an intensity of $30W/m^2$. Air was mixed with 203ppm of NO_2 in N_2, leading an initial concentration of 190ppm of NO_2 and sufficient O_2 and H_2O to promote generation of free radicals. After sealing the sample in the reaction chamber three cycles of vacuum (reaching 6.3mbar) followed by gas filling were undertaken in order to ensure total replacement the previous gas composition.

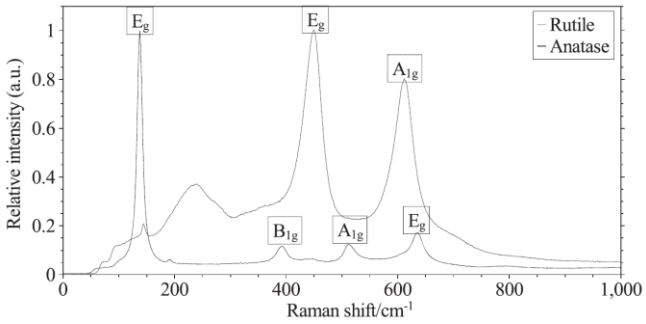

Figure 4. Raman Spectra of titanium dioxide crystal polymorphs.

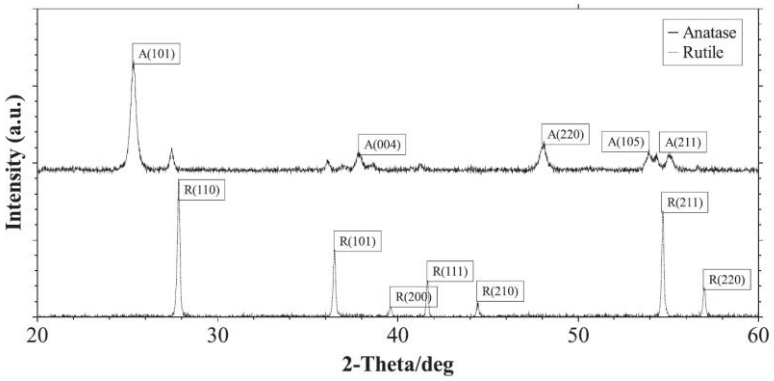

Figure 5. *XRD Spectra of titanium dioxide crystal polymorphs*

RESULTS AND DISCUSSION

The mass spectrum of a complex gas mixture can be approximated as the sum of the mass spectra of its individual components. The intensity of a given peak in the mass spectrum will be defined by the sum of all contributions in that mass-to-charge range. Figures 6 and 7 show an untreated spectrum obtained from a gas mixture comprising 190ppm of NO_2, 6% of air balance N_2 in the dark with no sample inside the chamber. Within this spectrum, the peak areas are related to the concentration for each molecule present in the gas mixture. The majority of the pressure within the system is due to N_2, and approximately 10^{-8} mbar. In order to identify the peaks corresponding to gases present in ppm quantities it is necessary to re-scale the pressure axis to show pressures in the range 10^{-10} mbar, as in figure 7. A peak at any given m/z value can comprise of one or more species, dependent on the gas composition and Table 1 contains details of the species which may contribute to the peaks identified.

The mass spectrum of pure NO_2 consists in four peaks with two minor peaks from atomic nitrogen and atomic oxygen (14m/z and 16m/z respectively); one peak for NO_2 at 46m/z and the most intense peak at 30m/z from NO^+. When the analysis gas contains molecular oxygen and molecular N_2, NO is formed due to the dissociative ionization of N_2 and O_2 by electron collision and subsequent recombination in the ioniser. The resolution of the mass spectrometer (better than 10% valley for peaks of equal height across mass range does not allow the exact mass of ions. Therefore a mass of 46m/z was followed during the reaction and assumed to reflect the proportion of NO_2. It should be noted that in doing this it is assumed that the contribution from other species with the same mass-to-charge ratio can be ignored. In the case of CO_2, the main peak is at 44m/z with additional peaks at 12m/z for C^+, 16m/z for O^+, 22m/z for CO_2^{2+}, 28m/z for CO^+, 29m/z for isotopic $^{13}CO^+$ and 45m/z for isotopic $^{13}CO_2^+$. The peak at 44 m/z will be referred to as the CO_2 peak and the same definition has been applied for peaks of 18m/z (H_2O), peak 28m/z (N_2), peak 32m/z (O_2) and peak 40m/z (Ar).

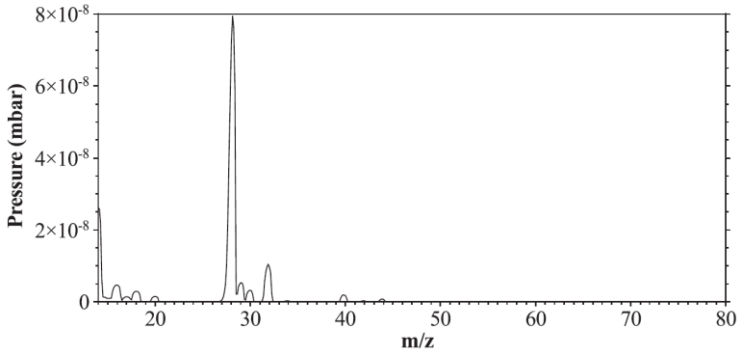

Figure 6. *Mass spectrum of the gas composition formed by 94%190ppm of NO_2, 6% of air balanced with N_2.*

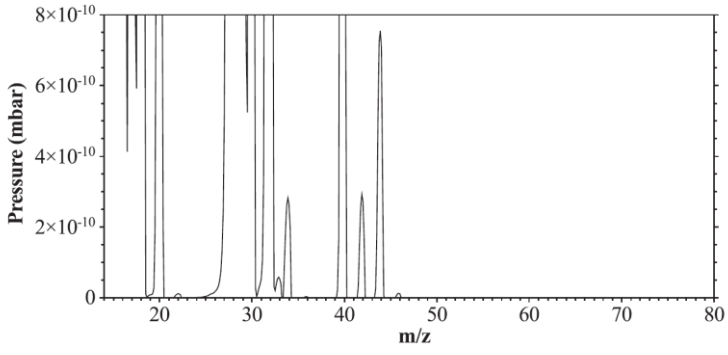

Figure 7. *Mass spectrum of 190ppm of NO_2, 6% of zero air grade balance N_2.*

Table 1: *Major ions in the 70eV EI mass spectra and the expected species of a gas mixture containing 190ppm of NO_2, 6% of air balance N_2 spectrum and their correlations with singular mass spectra of its components. Numbers in parenthesis show the relative intensity for the pure mass spectrum of an molecule.*

m/z	H_2O	CH_4	N_2	O_2	Ar	CO_2	NO_2
14		CH_2^+ (20.4%)	N^+ (13.8%)				N^+ (9.6%)
15		CH_3^+ (88.8%)					
16	O^+ (0.9%)	CH_4^+ (100%)		O^+ (21.8%)		O^+ (9.6%)	O^+ (22.3%)
17	OH^+ (21.2%)	CH_5^+ (1.6%)					
18	H_2O^+ (100%)						
19	H_3O^+ (0.5%)						
20	H_2O^+ (0.3%)				Ar^{++}(14.6%)		
22						CO_2^{++} (1.9%)	
28			N_2^+ (100%)			CO^+ (9.8%)	
29			$^{14}N^{15}N^+$ (0.8%)			$^{13}CO^+$ (0.1%)	
30			$^{15}N_2^+$				NO^+ (100%)
32				O_2^+ (100%)			
33				$^{16}O^{17}O^+$			
34				$^{16}O^{18}O^+$			
36				$^{18}O_2^+$	$^{36}Ar^+$ (0.3%)		
38					$^{38}Ar^+$ (0.05%)		
40					Ar^+ (100%)		
42							
44						CO_2^+ (100%)	
45						CO_2^+ (1.2%)	
46						CO_2^+ (0.4%)	NO_2^+(37%)
47							NO_2^+ (0.1%)

The partial pressure for any analyte can be calculated following the equation shown below

$$P_i = I \times \frac{Acs}{2.508\text{Å}^2} \times P \times \frac{ppm}{10^6} \quad (7)$$

Where *`I´* represents the relative intensity of the peak for the analyte; *`A_{CS}´* is the ionization cross-section of the analyte (in Å^2); *`P´* represents the total pressure of the system. 2.508 Å^2 is the ionization cross-section for N_2 at 70eV [41].

Microvision 2 reports that the ion current is converted to pressure using a single calibration point, and that there are no gas specific factors applied; therefore NO_2 can be calculated following the equation above. At 70eV the ionization cross-section for NO_2 is 3.532Å^2, thus, the relative ionisation sensitivity from NO_2 is 1.41. The total pressure inside the detector is 5.4×10^{-5} mbar, and the relative intensity of NO_2 for the 46m/z peak is 37% of the partial pressure:

$$P_{NO_2} = 0.37 \times 1.41 \times 5.4 \times 10^{-5} \times 2.0^{-4} = 5.6 \times 10^{-9} mbar \quad (8)$$

Referring back to Figures 6 and 7 which show the mass spectra for the gas mixture under study, the peak 46m/z has an intensity of 1.6×10^{-11} mbar. This is two orders of magnitude smaller than that predicted from equation 7. Additionally the peaks for H_2O and CO_2 are not related to their theoretical value if equation 7 is applied which suggests concentrations of 0.23 and 2.85 ppm for H_2O and CO_2 respectively. This observation is attributed to cross-sensitivity effects [42, 43], that can modify the sensitivity of the detector and for CO_2 the signal is greater and lower in the case of NO_2.

Previous researchers employing residual gas analysis to study gas mixtures used mathematical methods such as function-based least mean square regression [44, 45], parallel factor analysis [45] or the use of an internal standard [46]. However this approach can be problematic as Turner and colleagues have reported changes in the response of the detector with time due to the cross-sensitivity effects that species generated when in the same gas mixture [42]. Figure 8 shows the partial pressure of H_2O, O_2, CO_2 and NO_2 and compared to that of Ar which is plotted using a secondary y-axis. A comparison of the data indicates a similar curvature over the respective pressure ranges.

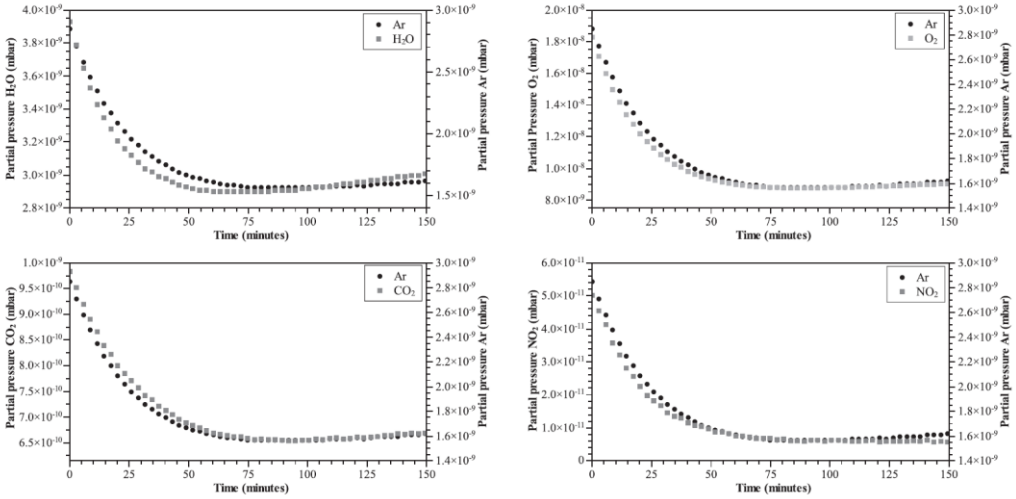

Figure 8. *Partial pressures of H_2O, O_2, Ar, CO_2 and NO_2 over time with the empty chamber in the dark. Right 'y' axis is fixed for Ar partial pressure whereas left 'y' axis shows the value for the species over 150 minutes. The gas mixture containing 190ppm of NO_2, 6% of air balance N_2 with the empty chamber in the dark.*

Figures 9, 10, 11 and 12 show the measurement for NO_2 and CO_2 processed through different data treatments; figure 7 shows the extracted data from the quadrupole mass filter expressed in mbar in which the primary y axis corresponds to the pressure of NO_2 and the secondary for Ar (in figure 9) and CO_2 in figures 10 and 11.

When a sample was held inside the system and a photocatalytic reaction occurred on its surface, the species did not follow the same trend; figure 9 shows the differences observed over 150 minutes when rutile is not irradiated and the reaction when rutile is irradiated with a UV source.

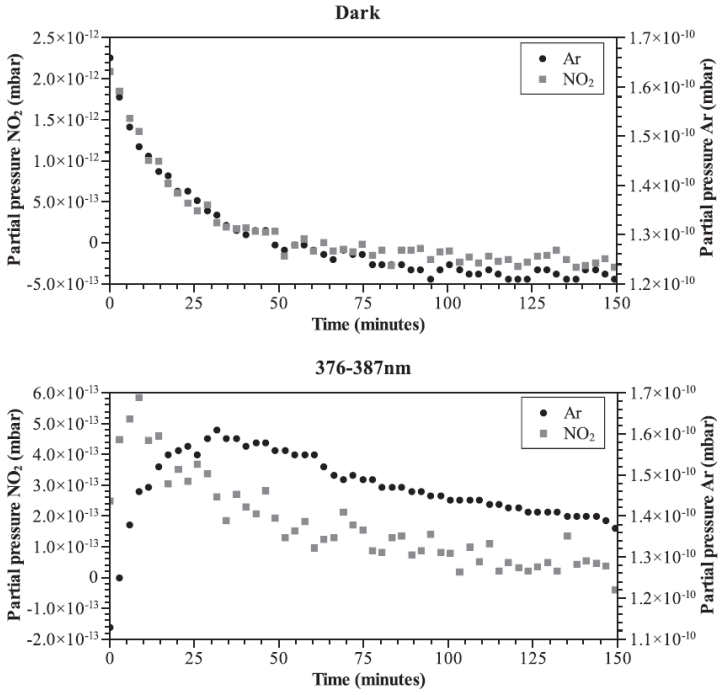

Figure 9. *Partial pressure of Ar and NO_2 over 150 minutes with rutile inside the chamber. Top graph shows the reaction in the dark and bottom graph shows the effects of rutile under UV irradiance. The gas mixture containing 190ppm of NO_2, 6% of air balance N_2. For both graphs left 'y' axis shows the relative intensity for NO_2; right 'y' axis shows the relative intensity for Ar.*

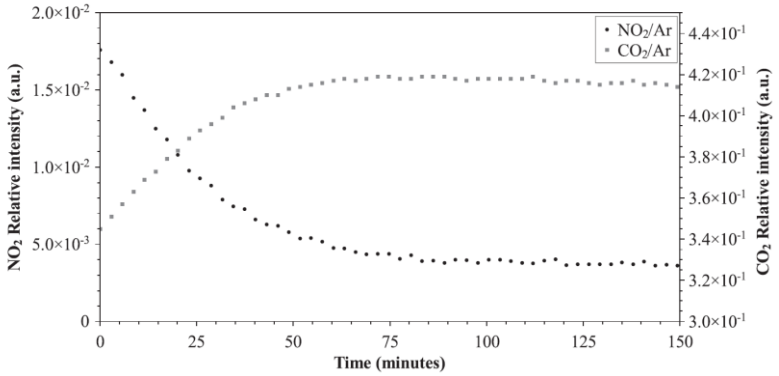

Figure 10: *Relative intensity of CO_2 and NO_2 normalized with the partial pressure of Ar over time with the empty chamber in the dark, the gas mixture containing 190ppm of NO_2, 6% of air balance N_2 with*

the empty chamber in the dark. Left 'y' axis shows the relative intensity for NO_2; right 'y' axis shows the relative intensity for CO_2.

In order to avoid derived errors from pressure fluctuations the measured data can be normalised relative to Ar which will be used as an internal standard and also absolute pressure. Due to the limited reactivity of Ar, it is used to track if there is any absorption process rather than photo degradation, the loss of intensity and therefore, most of the derived problems from the data collection will not affect the result. Figures 10 and 11 show the result of these treatments for CO_2 and NO_2; figure 10 shows values for CO_2 and NO_2 after being divided by the Ar partial pressure, whereas figure 10 shows the result of dividing by the total pressure. The results are identical, but instead of showing a stable signal, NO_2 decreases and CO_2 increases in intensity. Normalizing the data by the partial pressure of Ar or the absolute pressure distorts the real trend of NO_2. Figure 12-15 shows the value of H_2O, O_2, CO_2 and NO_2 after being re-scaled and compared to the trend that Ar follows.

A constant intensity would be helpful and allow comparisons to be made between different experimental conditions however a time-dependent interference is observed.

In this paper we report an alternative multiplicative approach which considers the fractional changes of the gas of interest and compares it to that of an inert internal standard (in this case Ar). This effectively considers the shape of the curve for the partial pressure of an element irrespective of the absolute pressure. The fractional change of Ar during the experiment is defined as α, where the superscript 'max' is the maximum value of its partial pressure for the data series; 'min' is the minimum value of its partial pressure for the data series and 'i' is the partial pressure value for a given time during the experiment.

$$\alpha = \frac{Ar^{max} - Ar^{i}}{Ar^{max} - Ar^{min}} \quad (9)$$

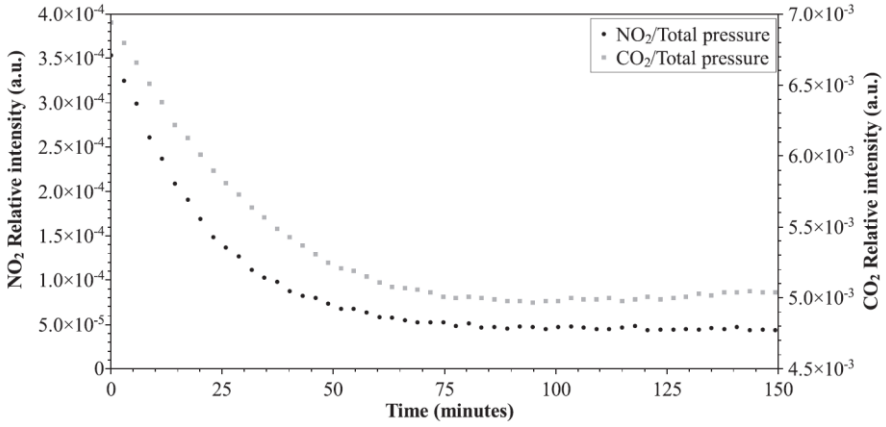

Figure 11: *Relative intensity of CO_2 and NO_2 normalized with total pressure over time with the empty chamber in the dark, the gas mixture containing 190ppm of NO_2, 6% of air balance N_2 with the empty chamber in the dark. Left 'y' axis shows the relative intensity for NO_2; right 'y' axis shows rhe relative intensity for CO_2.*

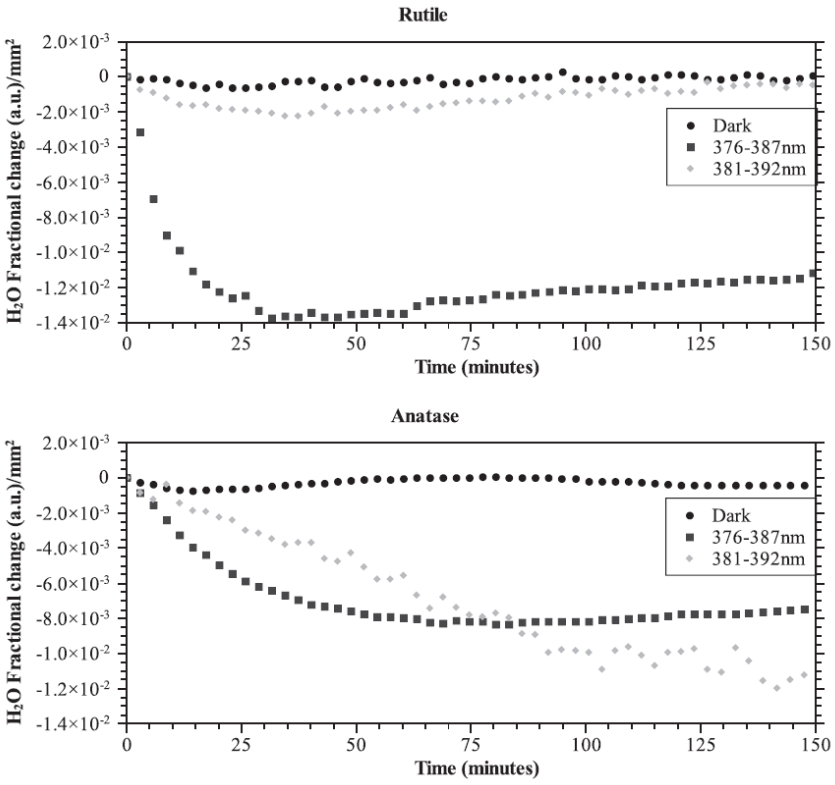

Figure 12: *Fractional reduction of H_2O related to Ar over time under different conditions.*

Table 2: *Average and standard deviation values for NO_2, O_2, H_2O and CO_2 over 150 minutes of reading values of a gas mixture containing 190ppm of NO_2, 6% of air balance N_2 with the empty chamber in the dark.*

	Average	**Standard deviation**
H_2O	1.26 x10^{-04}	4.18x10^{-04}
O_2	-1.12 x10^{-04}	1.23x10^{-04}
CO_2	1.25 x10^{-04}	1.09x10^{-04}
NO_2	-1.55x10^{-04}	1.26x10^{-04}

This treatment can be applied using similar methodology to the data relating to the m/z ratio of a molecule of interest, defined as X.

$$\varepsilon_X = \frac{X^{max} - X^i}{X^{max} - X^{min}} \quad (10)$$

ε_X represents the relative change of the molecule *'X'*. This treatment normalises the data to a value between 0 and 1. The fractional change of '*X'* considering the changes of Ar with time by mm^2 (area of the sample) in the Ar partial pressure scale is then defined as:

$$\underset{N}{^i}X = \frac{\varepsilon_X - \alpha}{Area} \quad (11)$$

The treatment has been applied to all data expressed by equations 9-11.

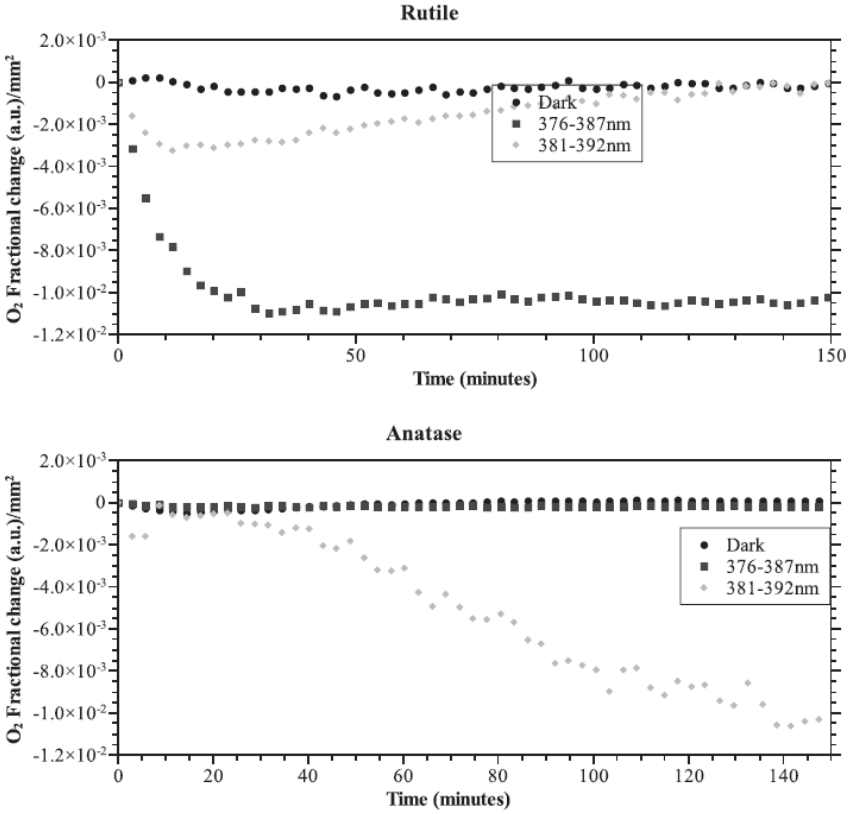

Figure 13: *Fractional reduction of O_2 related to Ar over time under different conditions.*

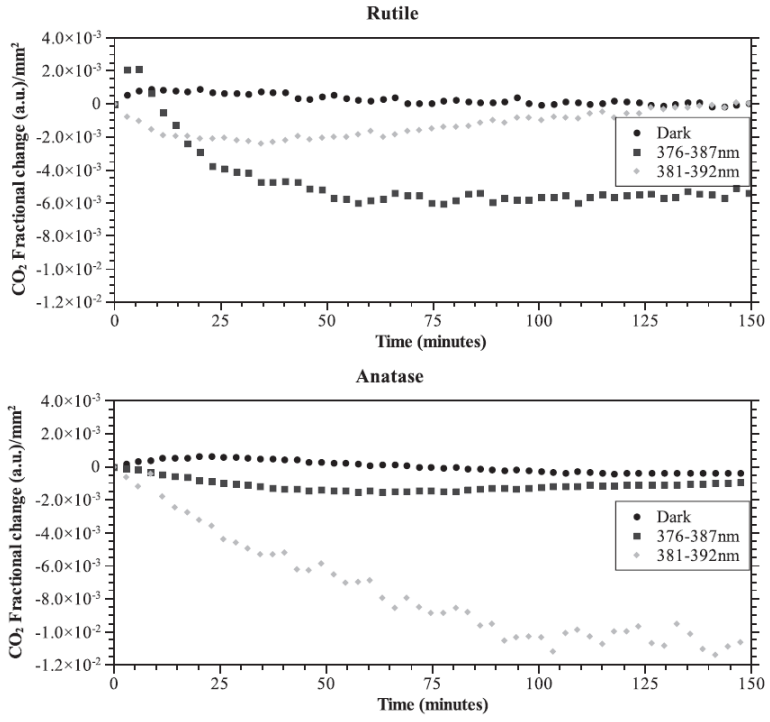

Figure 14: *Fractional reduction of CO_2 related to Ar over time under different conditions.*

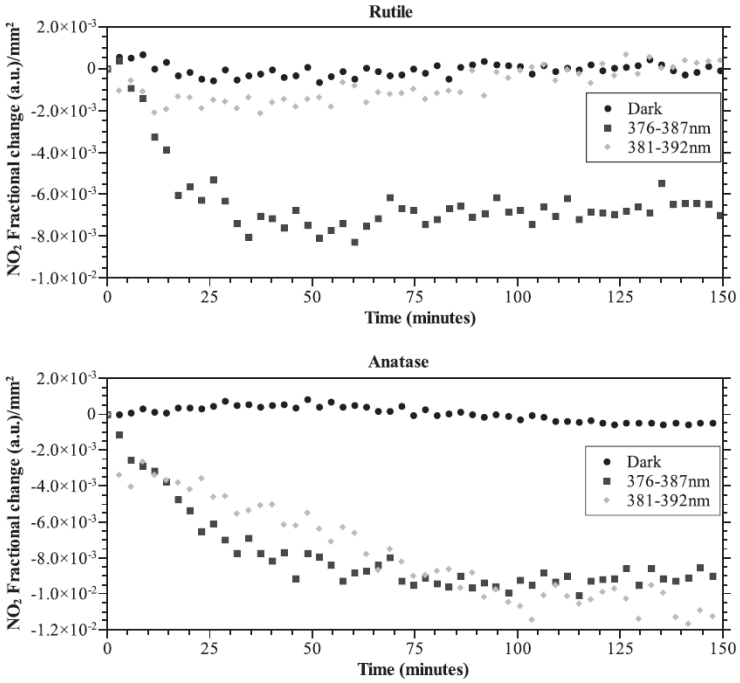

Figure 15: *Fractional reduction of NO_2 related to Ar over time under different conditions.*

Testing of an empty chamber

The reliability of the data treatment and the stability of the instrument despite of the cross-sensitivity effects were tested by carrying out an experiment with an empty chamber and replacing the quartz viewport for a stainless steel blanket to remove any potential photocatalytic effects. Although the lack of a sample inside the chamber would mean an area of $0mm^2$, equation 11 would equal infinitive, therefore an area was arbitrary set to that of experiments with a sample present ($132.73mm^2$)

The average values after applying this data treatment for NO_2, O_2, H_2O and CO_2 during 150 minutes and their standard deviations are shown in table 2. The data indicates only small fluctuations in value and provides a baseline to which data corresponding to reactions can be compared.

Testing of anatase and rutile

Anatase and rutile pellets were tested under different conditions: in the dark, under UV light of λ 376-387nm and λ 381-392nm for 150 minutes. Figures 12, 13, 14 and 15 show the evolution of H_2O, O_2, CO_2 and NO_2 when rutile and anatase are exposed to UV light or under darkness.

Comparing the results shown in figures 12-15, a fractional reduction of H_2O, O_2, CO_2 and NO_2 is observed. Anatase and rutile were able to promote a photodegradation of NO_2 and CO_2, consuming during the process H_2O and O_2. Anatase was more reactive under a UV irradiation of wavelength 381-392nm, whereas rutile was more reactive under a UV irradiation of a lower wavelength (λ 376-387nm).

When anatase was exposed to a UV source of λ 381-392nm with an intensity of 30W/m^2, CO_2 as well as NO_2 were degraded consuming H_2O and O_2, while on the contrary when the UV source with a lower wavelength was used, only NO_2 was removed.

Rutile did not show reactivity under a UV irradiation of λ 381-392nm. Although under an irradiation of λ 376-387nm the consumption of H_2O and O_2 was similar to the promoted reactions by anatase and it did reduce CO_2 as well as NO_2, albeit on a smaller scale.

In a number of cases, most readily observed for the anatase where little evidence of reaction is observed an increase in the NO_2 gas concentration is observed following a decrease in the short term. This is attributed to the release of absorbed gases.

Significant differences in the behaviour of TiO_2, especially in the rutile form, were observed under irradiation of different wavelengths. This is likely to be attributed to the absorption characteristics which are a function of properties such as structure, composition and surface morphology.

Conclusions

The following conclusions can be drawn from this study:

(i) The treatment of mass spectrometry data obtained from the study of gas phase photocatalytic reactions by normalising pressures by dividing by an internal standard such as argon, or the total pressure, can lead to misleading results attributed to cross-sensitivity effects. In these experiments this was shown by changes in CO_2 and NO_2 concentrations in experiments conducted in the dark were no reaction occurred.

(ii) A new protocol has been proposed which reduces errors from instability in the mass spectrometer over time by comparing the fractional change in the specie of interest to that of an internal standard such as argon.

(iii) The apparatus described allowed the control of important parameters such as light intensity and its spectrum, temperature and pressure. A residual gas analyser has proved to be stable in long term experiments with a resolution better than 10% valley for peaks of equal height across mass and detection limit of 0.2 ppb.

(iv) Results presented highlighted distinct differences in the photocatalytic activity of anatase and rutile polymorphs of TiO_2 under different conditions.

(v) Anatase promoted the photodegradation of CO_2 and NO_2 under λ 381-392nm.

(vi) Rutile was more reactive under λ 376-387nm compared to λ 381-392nm.

(vii) In the conditions that a reaction was not promoted, under UV irradiation, anatase and rutile did absorb those gases more than in the dark, being released after one hour.

(viii) The proposed system and approach provides a new methodology for the analysis and assessment of photocatalytic materials for air purification.

Acknowledgements

The authors acknowledge research funding from University of Bath and instrumentation funding from the Royal Society, Research grant RG110024. Thanks are also due to Professor W. N. Wang (University of Bath) for supplying the LEDs.

Bibliography

1. Solomon, S., D. Qin, M. Manning, Z. Chen, M. Marquis, K.B. Averyt, M. Tignor, H.L. Miller, *Contribution of Working Group I to the Fourth Assessment Report of the Intergovernmental Panel on Climate Change*, C. Cambridge University Press, United Kingdom and New York, NY, USA, 996 pp., Editor **2007**.
2. Utell, M. J., Frampton, M. W., Roberts, N. J., Jr., Finkelstein, J. N., Cox, C., Morrow, P. E., *Mechanisms of nitrogen dioxide toxicity in humans.* Res Rep Health Eff Inst, **1991**, *43*, 1.
3. Marilena Kampa, E.C., *Human health effects of air pollution.* Environmental Pollution. **2008**. *151***,** 2 362.
4. *Directive 2008/50/EC of the European Parliament and of the Council of 21 May 2008 on ambient air quality and cleaner air for Europe*, **21 May 2008**.
5. Fujishima, A. and K. Honda, *Electrochemical photolysis of water at a semiconductor electrode.* Nature. **1972**. *238*, 5358.
6. Primo, A., García H., *New and Future Developments in Catalysis*. Elsevier ed. **2013**.
7. Shieh, K.-J., Li, M., Lee, Y-H., Sheu, S-D., Liu, Y-T., Wang, Y-C. Antibacterial performance of photocatalyst thin film fabricated by defection effect in visible light. *Nanomedicine: Nanotechnology, Biology and Medicine.* **2006**. *2,* 121.
8. Dunnill, C.W.H., Aiken, Z. A., Pratten J., Wilson M., Morgan D.J., Parkin I. P., Enhanced photocatalytic activity under visible light in N-doped TiO2 thin films produced by APCVD preparations using t-butylamine as a nitrogen source and their potential for antibacterial films. *Journal of Photochemistry and Photobiology A: Chemistry*. **2009**, *207,* 244
9. Wei, S.-W., Peng B., Chai L.-Y, Liu Y.-C., Li Z.-Y., Preparation of doping titania antibacterial powder by ultrasonic spray pyrolysis. *Transactions of Nonferrous Metals Society of China*. **2008**, *18,* 1145.
10. Hochmannova, L. and Vytrasova J., Photocatalytic and antimicrobial effects of interior paints. *Progress in Organic Coatings*. **2010**. *67,* 1.
11. Fujishima A., Zhang X., Titanium dioxide photocatalysis: present situation and future approaches. *Comptes Rendus Chimie*. **2006**, *9,* 750.
12. Fujishima, A., Rao T.N., Tryk D.A. *Titanium dioxide photocatalysis. Journal of Photochemistry and Photobiology C: Photochemistry Reviews.* **2000,** *1*, 1.
13. Carp, O., Huisman C.L., Reller A., Photoinduced reactivity of titanium dioxide. *Progress in Solid State Chemistry*. **2004**. *32*, 33.
14. Amtout, A., Amtout R., and Leonelli, Optical properties of rutile near its fundamental band gap. *Physical review. B, Condensed matter*. **1995**, *51*, 6842.

15. Glassford, K.M., J.R. Chelikowsky. Optical properties of titanium dioxide in the rutile structure. *Physical Review B*. **1992**, *45*, 3874.
16. Kavan L., G.M., Gilbert S. E., Klemenz C., Scheel H. J. Electrochemical and Photoelectrochemical Investigation of Single-Crystal Anatase. *Journal of the American Chemical Society*. **1996.** *118*, 6716.
17. Asahi, R., Taga, Y., Mannstadt, W., Freeman, A. J. Electronic and optical properties of anatase TiO_2. *Physical Review B*. **2000**, *61*, 7459.
18. Egerton, T.A., Mattinson J.A. The influence of platinum on UV and 'visible' photocatalysis by rutile and Degussa P25. *Journal of Photochemistry and Photobiology A: Chemistry*. **2008**, *194*, 283.
19. Hoffmann, M.R., Martin, S. T., Choi, W., Bahnemann, D. W. Environmental applications of semiconductor photocatalysis. *Chemical Reviews*. **1995**, *95*, 69.
20. Fujishima, A., X. Zhang, and D.A. Tryk. TiO2 photocatalysis and related surface phenomena. *Surface Science Reports*. **2008**, *63*, 515.
21. Heller, A. Chemistry and Applications of Photocatalytic Oxidation of Thin Organic Films. Accounts of Chemical Research. **1995**, *28*, 503.
22. Serratos, M., Bronson A. The effect of oxygen partial pressure on the stability of Magneli phases in high temperature corrosive wear. *Wear*. **1996**. *198*, 267.
23. Berger T., Sterrer M., Diwald O., Knözinger E. Charge Trapping and Photoadsorption of O2 on Dehydroxylated TiO2 Nanocrystals—An Electron Paramagnetic Resonance Study. *ChemPhysChem*. **2005**, *6*, 2104.
24. Daimon, T., et al., Formation of singlet molecular oxygen associated with the formation of superoxide radicals in aqueous suspensions of TiO2 photocatalysts. Applied Catalysis A: General, 2008. 340(2): p. 169-175.
25. Maggos T., Bartzis J. G., Liakou M., Gobin, C. Photocatalytic degradation of NOx gases using TiO2-containing paint: A real scale study. *Journal of Hazardous Materials*. **2007**, *146, 668*.
26. Geng Q.-J., Wang X.-K., Tang S.-F. Heterogeneous Photocatalytic Degradation Kinetic of Gaseous Ammonia Over Nano-TiO2 Supported on Latex Paint Film. *Biomedical and Environmental Sciences*. **2008**, *21*, 118.
27. Kolarik J., Toftum J. The impact of a photocatalytic paint on indoor air pollutants: Sensory assessments. *Building and Environment*. **2012**, *57*, 396.
28. Oh W.-C., Zhang F.-J., Chen M.-L. Characterization and photodegradation characteristics of organic dye for Pt–titania combined multi-walled carbon nanotube composite catalysts. *Journal of Industrial and Engineering Chemistry*. **2010**, *16*, 321.
29. Tseng Y.H., Kuo C.H., Photocatalytic degradation of dye and NO(x) using visible-light-responsive carbon-containing TiO_2. *Catalysis Today*. **2011**, *174*, 114.
30. Mor, G.K., Varghese O. K., Paulose M., Shankar K., Grimes C. A. A review on highly ordered, vertically oriented TiO2 nanotube arrays: Fabrication, material properties, and solar energy applications. *Solar Energy Materials and Solar Cells*. **2006**, *90*, 2011.
31. Sampaio, M.J., Silva C. G., Marques R. N., Silva, A. M. T., Faria, J. L. Carbon nanotube–TiO_2 thin films for photocatalytic applications. Catalysis Today. **2011**, *161*, 91.
32. Ohno, T., TsubotaT., Nishijima K., Miyamoto Z. Degradation of Methylene Blue on Carbonate Species-doped TiO_2 Photocatalysts under Visible Light. *Chemistry Letters*, **2004**, *33*, 750.
33. Lin, C.Y., Fang Y. K., Kuo C. H., Chen S. F., Lin C.-S., Chou T. H., Lee Y.-H., Lin J.-C., Hwang S.-B. Design and fabrication of a TiO_2/nano-silicon composite visible light photocatalyst. *Applied Surface Science*. **2006**, *253*, 898
34. Zhu J., Ren J., Huo Y. N., Bian Z. F., Li H. X. Nanocrystalline Fe/TiO_2 visible photocatalyst with a mesoporous structure prepared via a nonhydrolytic sol-gel route. *Journal of Physical Chemistry C*. **2007**, *111*, 18965.
35. Ali, A.M., Emanuelsson E.A.C., Patterson D.A., Photocatalysis with nanostructured zinc oxide thin films: The relationship between morphology and photocatalytic activity under oxygen limited and oxygen rich conditions and evidence for a Mars Van Krevelen mechanism. *Applied Catalysis B-Environmental*. **2010**, *97*, 168.

36. Zhang F.-J., Chen M.-l., Oh W.-C., Photoelectrocatalytic properties of Ag-CNT/TiO2 composite electrodes for methylene blue degradation. *New Carbon Materials*. **2010**, *25*, 348.
37. Oh W.-C., Zhang F.-J., Chen M.-L., Synthesis and characterization of V–C60/TiO2 photocatalysts designed for degradation of methylene blue. *Journal of Industrial and Engineering Chemistry*. **2010**, *16*, 299.
38. Alonso, E., Montequi I., Cocero M.J., Effect of synthesis conditions on photocatalytic activity of TiO_2 powders synthesized in supercritical CO_2. *Journal of Supercritical Fluids*. **2009**, *49*, 233.
39. Gaffney J. S., Bornick R.M., Chen Y.-H., Marley N. A. Capillary gas chromatographic analysis of nitrogen dioxide and pans with luminol chemiluminiscent detection. *Atmospheric Environment*. **1998**, *32*, 1445.
40. Hernández-Fernández J. , Zanella R., Aguilar-Elguezabal A. ,Arizabalo R.D., Castillo S., Moran-Pineda M., Decomposition of NO in gas phase by gold nanoparticles supported on titanium dioxide synthesized by the deposition–precipitation method. *Material science and engineering B*. **2010**, *174*, 13.
41. Hwang W., Kim Y.K., Rudd M.E., New model for electron-impact ionization cross sections of molecules. *The Journal of Chemical Physics*, **1996**. *104*, 10.
42. Turner P., Clarke E. , Harwood C., Cooke K., Frampton H. Calibration effects during natural gas analysis using a quadrupole mass spectrometer. *Trends in Analytical Chemistry*. **2004**, *23*.
43. Lieszkovszky L., Filippelli A.R. Performance studies of partial pressure analysers. *Vacuum.* **1990**, *41*, 2142.
44. Ketola R. A., Ojala M., Komppa V., Kotiaho T., Juujärvi J., Heikkonen J. A non-linear asymmetric error function-based least mean square approach for the analysis of multicomponent mass spectra measured by membrane inlet mass spectrometry. *Rapid Communications in Mass Spectrometry*. **1999**, *13*, 654.
45. Gardner, W.P., Shaffer R. E., Girard, J. E., Callahan, J. H. Application of Quantitative Chemometric Analysis Techniques to Direct Sampling Mass Spectrometry. *Analytical Chemistry*. **2000**, *73*, 596.
46. Pérez Pavón, J.L., del Nogal Sánchez M., García Pinto, C., Fernández Laespada, M. E., Moreno Cordero B., Guerrero Peña A. Strategies for qualitative and quantitative analyses with mass spectrometry-based electronic noses. *Trends in Analytical Chemistry*. **2006**, *25*, 257.